IEEE Open Journal of
Intelligent Transportation
Systems

Received 10 February 2022; revised 6 April 2022; accepted 27 April 2022. Date of publication 19 May 2022; date of current version 3 June 2022.

*Digital Object Identifier 10.1109/OJITS.2022.3176471*

# Automotive Lidar and Vibration: Resonance, Inertial Measurement Unit, and Effects on the Point Cloud

**BIRGIT SCHLAGER[1,2], THOMAS GOELLES[1], MARCO BEHMER[3], STEFAN MUCKENHUBER[1,4], JOHANN PAYER[3], AND DANIEL WATZENIG[1,2]**

[1]Department of Automotive Electronics and Software, Virtual Vehicle Research GmbH, 8010 Graz, Austria

[2]Institute of Automation and Control, Graz University of Technology, 8010 Graz, Austria

[3]Department of NVH and Information Systems, Virtual Vehicle Research GmbH, 8010 Graz, Austria

[4]Department of Geography and Regional Science, University of Graz, 8010 Graz, Austria

CORRESPONDING AUTHOR: B. SCHLAGER (e-mail: birgit.schlager@v2c2.at)

This work was supported in part by the University of Graz; in part by the COMET K2 Competence Centers for Excellent Technologies from the Austrian Federal Ministry for Climate Action (BMK); in part by the Austrian Federal Ministry for Digital and Economic Affairs (BMDW); in part by the Province of Styria (Dept. 12); and in part by the Styrian Business Promotion Agency (SFG). The Austrian Research Promotion Agency (FFG) has been authorized for the Programme Management.

This article has supplementary downloadable material available at https://doi.org/10.1109/OJITS.2022.3176471, provided by the authors.

**ABSTRACT** Lidar is an important component of the perception suite for automated systems. The effects of vibration on lidar point clouds are mostly unknown, despite the lidar's wide adaption and usual application under conditions where vibration occurs frequently. In this study, we performed controlled vibration tests from 6 to 2000 Hz at 9 and 12 m/s$^2$ in vertical direction on the automotive lidar OS1-64 by Ouster. An information loss emerged which is mostly independent from frequency and acceleration. The loss of points is randomly distributed and does not correlate with range, intensity, or ring number (the horizontal line of the rotating lidar unit). The resonance frequency of 1426 Hz proved to be unproblematic as no pronounced negative effects on the point cloud could be identified. For vibration detection, the internal Inertial Measurement Unit (IMU) of the OS1-64 is accurate and sufficient for vibrations up to 50 Hz. Above 50 Hz, external IMUs would be required for vibration detection. Counting the number of points on a target close to the edges was investigated as an exemplary way to detect vibration purely based on the point cloud, i.e., independent of the lidar's IMU.

**INDEX TERMS** Automated vehicle, measurement errors, vibration measurement, vision sensors for intelligent vehicles.

## I. INTRODUCTION

PERCEPTION sensors are a key component for automated vehicles and indeed the quality of the entire environment recognition pipeline depends on them [1]. Hence, the capability of the vehicle depends largely on the reliability of these perception sensors. Lidar sensors are an essential component of a typical environmental perception suite. Lidar hardware and associated software components of the environment recognition pipeline have been improved in recent years, as the manufactures are competing to gain a share in this new and promising market. Consumers and shareholders alike insist on having vehicles for driving automatically under less than ideal conditions. This necessitates fault handling of the environment recognition pipeline, again starting at the perception sensors. One cause of such faults is vibrations, which strongly depend on the mounting solution on the vehicle chassis.

Two causes of vibrations of vehicles occur in the real world: rough road surfaces, e.g., road bumps, and vibrating components in the vehicle, e.g., electric motors. Gravel causes vibrations of up to 60 Hz and asphalt up to 150 Hz for example, while electric components cause higher frequencies.

The review of this article was arranged by Associate Editor Fernando Auat Cheein.

In a review paper from 2020, we classified faults and identified knowledge gaps for lidars [2]. There are only a few studies dealing with vibration-related problems caused by lidars. None of them analyzed the effects of vibrations on the resulting point cloud and most of them focused on mitigating the vibration effects of lidar subcomponents. Two studies [3] and [4] investigated the effects on Micro-Electro-Mechanical Systems (MEMS) based lidars. Both studies used shakers to apply vibrations to the micromirrors. They focused on the MEMS unit and did not test a complete lidar unit, nor was fault detection considered. Another study investigated a complete lidar unit under real conditions on an agricultural vehicle with the goal of developing a stabilizing unit [5]. They used a SICK LMS 291-S14 lidar with an internal rotating mirror, which, in the meantime, has been phased out by the manufacturer. This unit produced a position error of up to 27% with increasing tractor speed. Wang *et al.* [6] developed compensating methods for Frequency-Modulated Continuous Wave (FMCW) lidars, which are especially sensitive to vibrations. Cao *et al.* [7] used finite-element based analysis of a rotating lidar setup. They found that in their specific mechanical setup, resonance did not occur because the resonance frequency was above the typical frequency on a car. In addition, the mirror deformation due to vibrations was found to be about 0.0001°.

Vibration is also a problem for other perception sensors. In the following paragraph, we will briefly present some examples from vibration studies with automotive radar sensors. Harter and Hildebrandt [8] classified vibrations into three classes: *environmental vibration and shock* which concerns the complete sensor unit, i.e., housing, electronics, and connectors, *impact sound* due to sound being transferred from the chassis or other components to the sensor, and due to *vibration interaction between sensor fixture and cover* which is the relative movement between sensor and cover as a result of vibration. They used a shaker to excite a radar in a vertical fashion and found that the angle deviation lies between $-0.1°$ to $0.2°$, which is negligible for automotive radar. Hau *et al.* [9] simulated vibrations of an automotive chirp-sequence FMCW radar. This was followed by a more thorough study [10], where they developed the theory further and used a shaker to introduce sinusoidal movement.

The effect of vibration on lidar was also investigated considering non-automotive lidar systems. References [11] and [12] deal with vibration problems of airborne lidar and Doppler wind lidar. Ma and Wu [11] derived an estimate of the effect of vibrations on the accuracy based on geometric considerations. Again, the goal in [12] was to develop a mechanical stabilization system.

In [5], a vibration isolator was chosen based on the characteristics of the vibration, i.e., frequencies and load capacities, the geometry, material properties, and the mounting position of the lidar. We expect the final point cloud to be affected by these parameters, but it also depends on the internal signal processing. The exact mechanical properties and type of signal processing are usually unknown to third parties. Lidar manufacturers are very protective of their intellectual property, as automotive lidar is a very competitive emerging market. Against this backdrop, we are investigating the effects of vibrations on the final point cloud to identify problems and to pinpoint possibilities for detecting and isolating the faults automatically. Related work focuses on FMCW or MEMS lidar sensors or parts of these lidar technologies whereas our experiments focus on a pulsed time-of-flight rotating lidar sensor. Compared to previous work that concentrates especially on mechanical deformation of lidar sensors that highlights the problems caused by vibrations, we evaluate the influence of vibrations on the sensor data, i.e., point clouds and Intertial Measurement Unit (IMU) data. In the present work, we use a 64-line rotating automotive lidar by Ouster (OS1-64) as an example. Note that the exact problems might be specific to this lidar type, but the general approach and test setup may be applied to any automotive lidar. The manufacturer tests the fatigue limits of the lidar sensors by applying loads of up to $30\,\mathrm{m\,s^{-2}}$ [13]. However, the tests are not designed to evaluate how the functionality of the lidar sensors is affected during vibration. We address this gap in the present work.

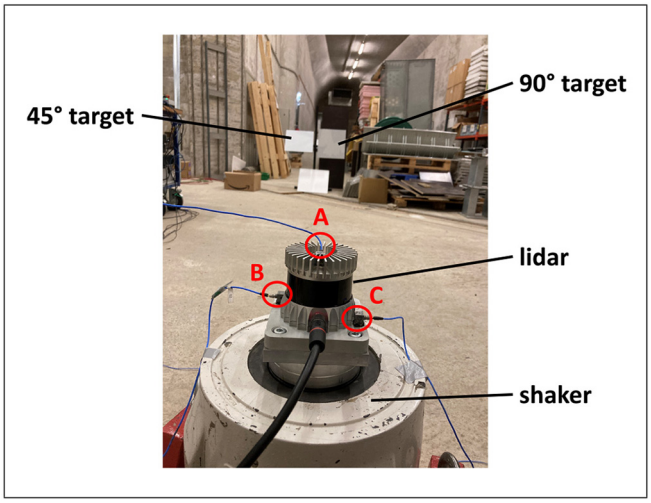


**FIGURE 1.** Measurement setup for vibration measurements. The red markers show the positions of the accelerometers.

The paper is structured as followed: Section II describes the measurement setup. Section III describes the methods used for data analysis of the point clouds and IMU. Section IV presents the results, while peripheral results are presented in the accompanying supplements. Finally, in Section V, we draw conclusions based on the results and discuss potential future research.

## II. MEASUREMENT SETUP

Fig. 1 shows the measurement setup consisting of the automotive lidar OS1-64 mounted on a shaker and the targets in the background. The lidar is excited only vertically by

**TABLE 1. Overview of frequencies and accelerations used for vibration excitation. Reference was measured on day 1. Day 1 was on December 2nd, 2020 and day 2 was on December 3rd, 2020.**

| Frequency (Hz) | $9\,\mathrm{m\,s^{-2}}$ | $12\,\mathrm{m\,s^{-2}}$ |
|---|---|---|
| 6 | day1 | day2 |
| 7 | day1 | day2 |
| 8 | day1 | day2 |
| 9 | day1 | day2 |
| 10 | day1 | day2 |
| 11 | day1 | day2 |
| 12 | day1 | day2 |
| 24 | day1 | |
| 48 | day1 | |
| 96 | | day1 |
| 192 | | day1 |
| 384 | | day1 |
| 768 | | day1 |
| 1536 | | day1 |
| 2000 | | day1 |

the shaker with the frequencies and acceleration outlined in Table 1. The acceleration was recorded by three triaxial accelerometers. Two accelerometers are located on the base plate (*B*, *C*) and one is located on the top of the OS1-64 (*A*). The measurements were taken in a large underground facility with neon lights as the only light sources.

The following subsections describe the lidar, vibration excitation, the targets, and the software including time synchronization in more detail.

### A. LIDAR: OUSTER OS1-64

The automotive lidar Ouster OS1-64 Gen1 (firmware version 1.13) used has the following specifications [14]:

- Range accuracy: zero bias for lambertian targets, slight bias for retroreflectors
- Horizontal resolution: 2048
- Vertical resolution: 64
- Angular sampling accuracy (vertical and horizontal): $\pm 0.01°$
- Rotation rate (point cloud sampling rate): 10 Hz
- Data per point: range, intensity, reflectivity, ring channel, noise, timestamp
- Built-in IMU type: InvenSense MPU9250 with 3 axis gyro and 3 axis accelerometer
- Built-in IMU sampling rate: 100 Hz
- Vibrations during operation: IEC 60068-2-64 with 10 to 1000 Hz at max. 3 g (RMS)
- Shock during operation: IEC 60068-2-2 with 100 g (peak)

The OS1-64 was bolted to the shaker-head expander at four mounting points at the corners of its base plate in the same way as it would be mounted on a vehicle.

### B. VIBRATION EXCITATION

The following hardware was used for the shaker setup:

- Shaker: Brüel & Kjær LDS V555
- Acceleration sensors: PCB Model 356B21 with a sensitivity of $10\,\mathrm{mV\,g^{-1}}$
- Vibration control and acquisition hardware: Siemens SCADAS Mobile 3.

To guarantee the functionality and safe operation of electronic vehicle components within the expected service life, so-called environmental tests are often conducted. A few standardized test protocols are established, e.g., ISO-16750-3, ISO 12405-2, which define the boundary conditions such as ambient temperature, frequency range, loads (accelerations), load direction, and the current clamping situation of the component in the vehicle.

In general, vibration tests can be performed with harmonic, i.e., sinusoidal, or stochastic, i.e., random signals. Both are part of environmental testing regulations and norms. Random broadband excitation is the closest to the kind that occurs in real vehicles and thus represents the excitation of uneven road and by road bumps. However, the sinusoidal vibration load allows better identification of the trajectory precision than random vibration [4]. For that reason, we use sinusoidal signals, since their influence on point clouds is more comprehensible than for random signals. With sinusoidal excitation, only one frequency is excited at a time, which leads to a specific deflection at defined excitation frequency and acceleration and thus makes it possible to determine the functional limits of the lidar being investigated. We consider the convention from [15], where displacements are given as peak-to-peak values and velocities as well as the accelerations as peak values.

The vertical direction is usually specified as the one with the highest acceleration levels in the available standards for vibration tests. This is since the vehicle and its components experience the greatest acceleration amplitudes in the vertical direction because of bumps and uneven road surfaces. Measurements on the bumpiest road in Dresden show that the maximum amplitude in the vertical direction is 0.36 g [4]. The primary goal when choosing the frequencies and accelerations is to find faults in the resulting point clouds. The measurement plan is therefore optimized for high deflection and not for realistic profiles. Based on current standards, e.g., ISO-16750, a frequency range of up to 2 kHz is typical for testing the functional safety of electrical components. For that reason, we use a frequency range from 6 Hz to 2 kHz, where 6 Hz represents the lower operating limit of the electrodynamic shaker used for excitation. Broadband excitation pre-tests served to detect prominent excitation frequencies for the following step sine tests. The mechanical tests were conducted with $9\,\mathrm{m\,s^{-2}}$ and $12\,\mathrm{m\,s^{-2}}$ in the vertical direction at room temperature. The two defined excitation levels in $\mathrm{m\,s^{-2}}$ are far below the operational limit of $29.4\,\mathrm{m\,s^{-2}}$ which equals to 3 g. However, the chosen excitation levels are over two times higher than the maximum amplitude of 0.36 g measured on the bumpiest road in Dresden [4] since this maximum amplitude equals to $3.5\,\mathrm{m\,s^{-2}}$. In conclusion, we chose the accelerations between the maximum acceleration

measured in [4] but far below fatigue limits of the sensor. Hence, the accelerations chosen are sufficiently large for testing the functionality of the sensor and small enough to avoid damaging the sensor.

### C. TARGETS

We used two 46 cm × 46 cm flat retroreflective static targets at a distance of about 6 m. Retroreflective targets are common in real road scenarios as signs and reflectors are retroreflective. One target was mounted in 45° and the other one in 90° to the floor. In addition to the two main targets, we distributed circular retroreflective targets with a diameter of 5 cm which were used for point cloud registration as described in Section III-A.

### D. SOFTWARE AND TIME SYNCHRONIZATION

We used the Robot Operating System (ROS) [16] for lidar and IMU data collection provided by the OS1-64 unit and the Siemens TestLab 2020 for data collection and controlling of the shaker and of accelerometers. Time synchronization between the two data collection systems was implemented using a digital signal for ROS and an analog signal for TestLab. This signal was provided by the push of a key from a music synthesizer, which provided an analog trigger signal together with a digital Musical Instrument Digital Interface (MIDI) message. The MIDI message was recorded at 100 Hz, and the analog signal at 10 000 Hz resulting in a maximum deviation of 10 ms between the two systems. The ROS timestamps were taken directly from the ROS messages, as this provided the best results.

## III. METHODS AND PROCEDURES

### A. REFERENCE MEASUREMENTS

Reference data, i.e., the exact 3D position of the targets, are required in order to quantify negative effects caused by the vibration. For that purpose, we employed two approaches: a plane equation derived from a high-precision terrestrial laser scanner and a mean point cloud derived from measurements at rest.

#### 1) REFERENCE POINT CLOUD

The reference point cloud was derived from a static measurement with 1,000 frames with our python package called *pointcloudset* which is available on PyPI (https://pypi.org/project/pointcloudset/) [17]. We isolated the center area of the 45° target in order to avoid edge effects, leaving 79 points on the target which were used to calculated the mean value of the coordinates for each individual point over the 1,000 frames.

#### 2) PLANE EQUATION

We used the high-precision terrestrial laser scanner VZ-6000 by RIEGL [18] to derive a plane equation of the targets. The VZ-6000 was placed just above the shaker position, where the OS1-64 was located during the measurement campaign. Then, a high-precision 3D point cloud of the area of interest — including the test targets and the surrounding environment — was recorded. The proprietary point cloud format of RIEGL (.rxp) was converted into an open format (.las) using RiSCAN PRO [19]. The open source software CloudCompare was then used to spatially transform the VZ-6000 point cloud into the coordinate system of the OS1-64. Automatic registration provided poor results. To make amends, the point cloud registration was performed manually. All VZ-6000 points that could be associated with the target were extracted and a plane representing the least squares solution of all remaining points was fitted with *pointcloudset* accordingly.

### B. MODAL ANALYSIS AND CALCULATION OF THE DISPLACEMENT

For a comparison of the recorded OS1-64 displacements, the accelerations recorded at the lidar's top enclosure (accelerometer $A$) need to be integrated twice. It follows then, that the acceleration measured is directly related to the displacement and can be determined by suitable numerical integration [20], see Appendix.

### C. LIDAR DATA ANALYTICS AND FAULT DETECTION

We waited until the steady state of the vibrating system before we started collecting data. We chose a recording time of 30 s per measurement since the slowest measurements with 6 Hz have 180 periods during this time, and this is enough for our statistical evaluations in a steady state of the system. Specifically, 30 s of recording time means that we are recording 300 point clouds per experiment at 10 Hz sampling frequency. We evaluate the 300 point clouds per experiment with *pointcloudset*.

A special processing step is necessary to evaluate the effects of the vertical displacement on the point cloud since the whole coordinate system of the lidar moves with the unit. Hence, on a vertical target alone, it is not possible to detect any changes in the distances from the perceptive of the vertically moving lidar. For that reason, a tilted target is necessary that serves as an encoding method for calculating the movement in z-direction from the $x$ values measured. The choice of the angle of the tilted target is a trade-off between more accurate range measurements but with less influence of the lidar displacement on $\Delta x$ for steeper targets. This choice furthermore features less accurate range measurements but more influence of the lidar displacement on $\Delta x$ for more flat targets. We use a 45° target. Fig. 2 shows the calculation of the shaker displacement in $z$ based on the measured $x$ values. During rest, the OS1-64 is at position 1, and during vibration, at position 2, as an example. The difference between the $x$ value of the reference position 1 and the $x$ value of the current position 2 in $z$ equals $\Delta x$, which is proportional to $\Delta z$.

### D. GEOMETRY

Some geometric considerations are required in order to interpret the results. The OS1-64 consists of 64 vertical

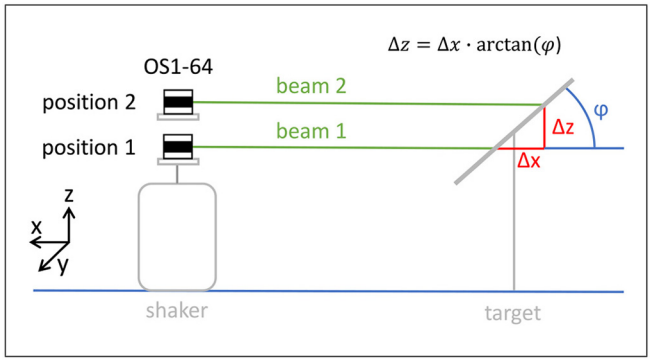


**FIGURE 2.** Determination of $\Delta z$ by using a 45° target and the measured x values.

lines [21] and as the scanner rotates, 64 horizontal *rings* are recorded. They are numbered from 0 to 63 and the distance between them can be calculated by:

$$d_{\text{rings}} = 2 \cdot d_{\text{target}} \cdot \tan\left(\frac{\pi}{180} \cdot \frac{\alpha}{2}\right) \tag{1}$$

resulting in 5.52 cm at 6 m distance. Where $d_{\text{rings}}$ is the distance between two rings, $d_{\text{target}}$ is the distance between the OS1-64 and the targets. The angle $\alpha$ between two beams can be calculated in the following way:

$$\alpha = \frac{FOV_{\text{vertical}}}{N_{\text{beams}} - 1} = \frac{33.2°}{63} = 0.53°, \tag{2}$$

where $FOV_{\text{vertical}}$ is the vertical field of view and $N_{\text{beams}}$ is the number of beams in vertical direction.

## IV. RESULTS

### A. STRUCTURE OF THE RESULTS SECTION

First, we present an analysis of the vibration excitation and of the resonance frequencies. This serves as a basis for interpreting the effects on the point cloud. Afterwards, we evaluate the OS1-64 internal IMU and continue with the core topic of this study — the evaluation of vibration effects on the point cloud and target detection. With this topic in mind, we will continue with a presentation of the reference point clouds consisting of the whole scene and the two targets.

All of the point cloud analytics plots use the same color scheme for the frequencies with two distinct markers for the accelerations. In addition, we included small icons at the top to give a quick idea about the reference and analytics methods employed. Note that all presented box plots show also outliers.

### B. MODAL ANALYSIS AND DISPLACEMENT

Fig. 3 shows that the displacement and velocity are higher at lower frequencies. As a result, a vertical shift in the point cloud can be expected in case of frequencies of up to 10 Hz. At higher frequencies, especially above 1000 Hz, the acceleration is the dominant driver.

Next, we looked into resonance frequencies in Fig. 4, where one resonance frequency at 1425 Hz could be identified. Frequencies close to this resonance were selected (Table 1) for possible multiplication of the deflection and hence possible distortion in the point cloud.

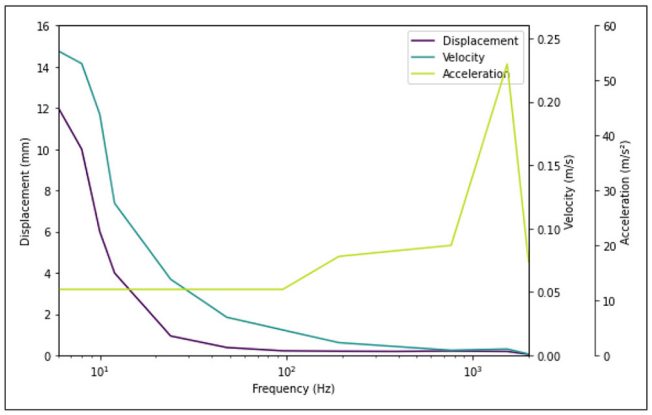


**FIGURE 3.** Acceleration and their derivatives, i.e., velocity and displacement, recorded by accelerometer *A*. Analyzed from 6 Hz to 2 kHz with a load of 12 $ms^{-2}$. Displacements are shown as peak-to-peak values, while velocities and accelerations are shown as peak values.

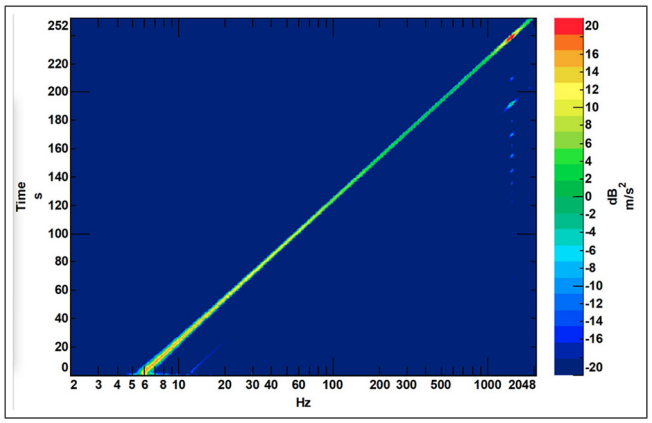


**FIGURE 4.** Harmonic sine sweep run from 6 Hz to 2 kHz, revealing resonance of the OS1-64 enclosure at 1425 Hz.

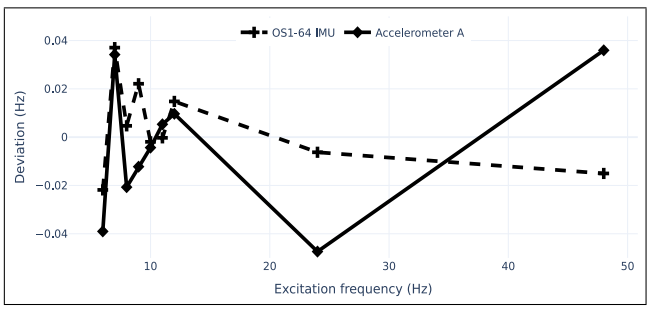


**FIGURE 5.** Deviation between the dominant frequencies of the accelerometer *A* and the OS1-64 IMU plotted over the target frequencies.

### C. EVALUATION OF THE IMU

We evaluated the IMU data of the OS1-64 and how they compare to the lab-grate accelerometers. For this purpose, we applied Fast Fourier Transforms (FFTs) to the lidar unit's IMU data. Fig. 5 shows that the deviation from the theoretical excitation frequency is low for both the accelerometer *A*

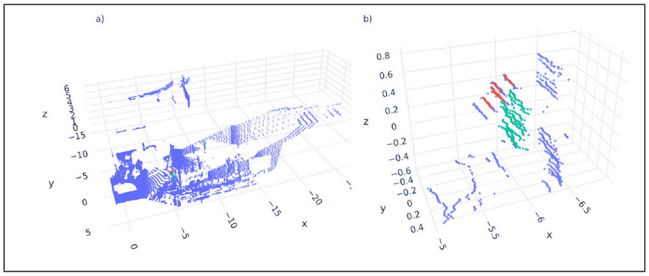


**FIGURE 6.** Overview point cloud of the whole scene recorded by the OS1-64, with the 45° target in red and the 90° target in green in panel a) and a zoom in panel b).

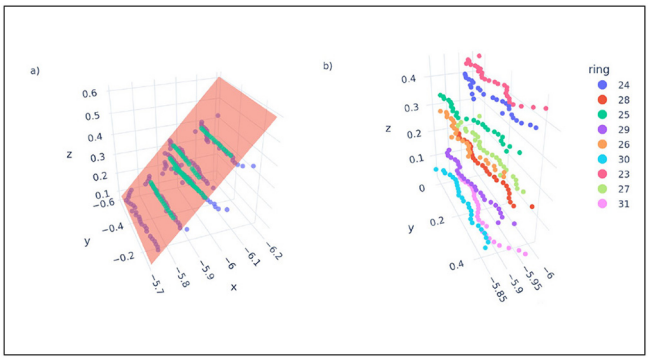


**FIGURE 7.** Panel a) shows the 45° target, where the reference plane is in red, the reference point cloud in green and an example OS1-64 point cloud in blue. Panel b) shows the 90° target and its ring numbers. Both targets are shown from the same line of sight as in Fig. 6.

and the OS1-64 IMU. This is despite the fact that, this is only possible for vibrations of up to half the sampling frequency of the IMU unit (100 Hz, see also Fig. S1 in the supplements).

### D. REFERENCE POINT CLOUDS AND PLANE

Fig. 6 shows the point cloud of the whole scene without vibration, with points as far away as 35 meters, while Fig. 7 takes a closer look at the 45° and 90° target as recorded by the OS1-64. The red plane in the 45° target was derived from the VZ-6000 measurements, with an angle $\varphi$ of 46.71° between the target and the floor. Note the offset from the plane on both targets. The offset is consistent from frame to frame, with a standard deviation ranging from 0.002 m to 0.021 m per point. The deviation error is relatively high, since the OS1-64 yields higher errors when measuring retroreflective targets (as added in the updated datasheet [22]). Additionally, when looking at the reflector foil from a larger angle, horizontal stripes with different intensities appear that are not visible to the human eye but detectable with a time-of-flight camera (see Fig. S2 in the supplements). These stripes did not affect the RIEGL VZ-6000 measurements, but could have an impact on automotive lidar systems, such as the OS1-64.

The center of the 45° target was chosen as the main reference. Points close to the edge are not considered to avoid edge effects. These center points were then averaged

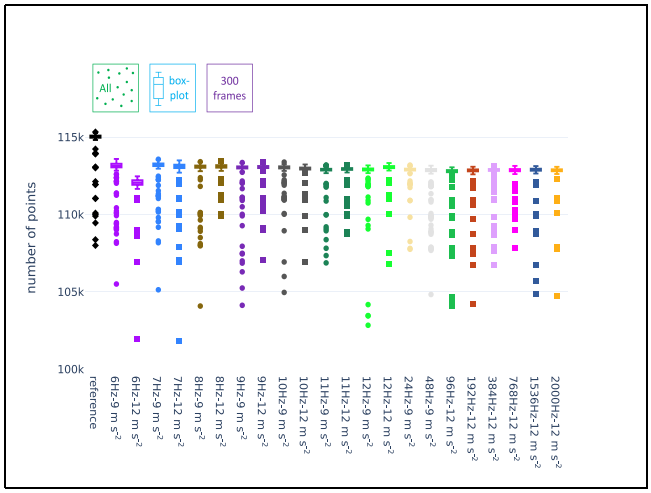


**FIGURE 8.** Number of points over the whole scene for 300 frames.

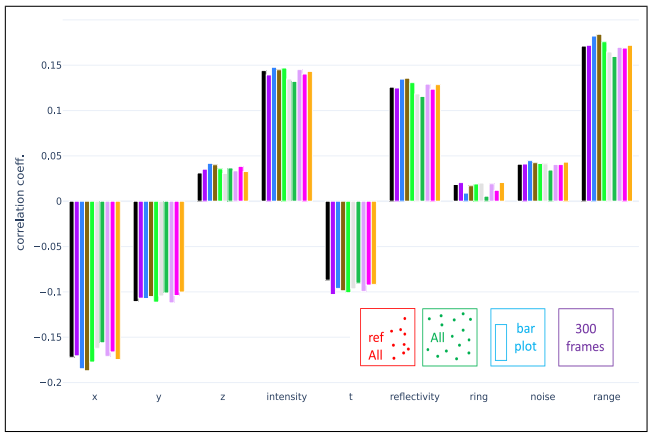


**FIGURE 9.** Correlation of the count of each point in the dataset, with lidar parameters for 9 $ms^{-2}$. Color scheme is the same as in Fig. 8, i.e., black is the static reference.

over 1,000 frames for the reference dataset, shown in green in Fig. 7a.

### E. EFFECTS OF VIBRATION ON THE POINT CLOUD OF THE COMPLETE SCENE

Fig. 8 shows the number of points per point cloud which have non-zero values. The theoretical maximum is 131,072 due to 64 beams facing in the vertical direction and 2,048 horizontal sampling positions. The reference has about 115,300 points while other experiments have between 111,000 and 113,500 per point cloud. Experiments at 6 Hz with the largest deflection have the highest number of dropouts and therefore the lowest number of points per point cloud. Fig. 9 shows that the correlation between the number of dropouts per point and the location of the points (x, y, and z) or other attributes of the points is low. It also shows that there is no difference between the static reference measurement in black and the vibration experiments in terms of correlation between dropouts and the attributes of the points. In conclusion, the number of dropouts increases during vibration, but

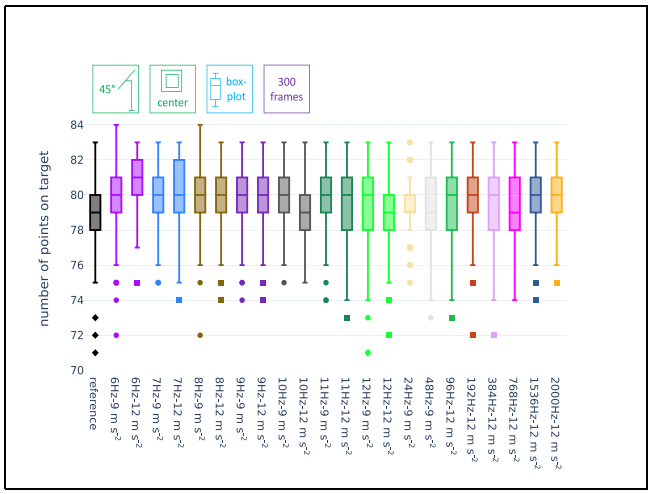


**FIGURE 10.** Number of points on the 45° target center over 300 frames.

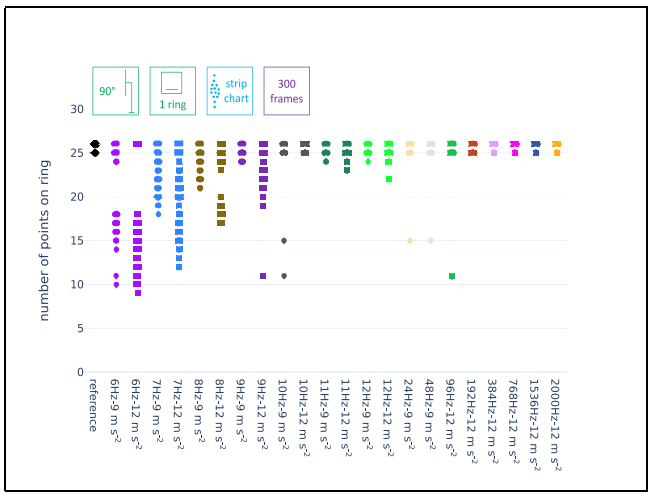


**FIGURE 11.** Number of points on the lowest ring (ring number 31) on the 90° target over 300 point clouds.

the dropouts show no correlation to the point location or to the values recorded per point. The information loss during vibration, moreover, is mostly independent of the excitation frequency and acceleration.

Fig. 10 takes a closer look at the center of the 45° target. The reference has a comparatively low number of points and no clear trend is visible. Most of the frames have between 78 and 83 points on the target.

### *F. EFFECTS OF VIBRATION ON THE POINT CLOUD OF THE TARGETS*

Next, we evaluated whether points of the upper or lower ring on the 90° target drop off while vibrating in Fig. 11. To that end, we analyzed the number of points on the target per ring for each frame (see also Fig. 7b).

Fig. 11 shows the number of points on the lowest ring, i.e., ring number 31 (see also Fig. 7b). In the static reference, there are either 25 or 26 points of this ring on the target. All experiments have some frames with the same numbers

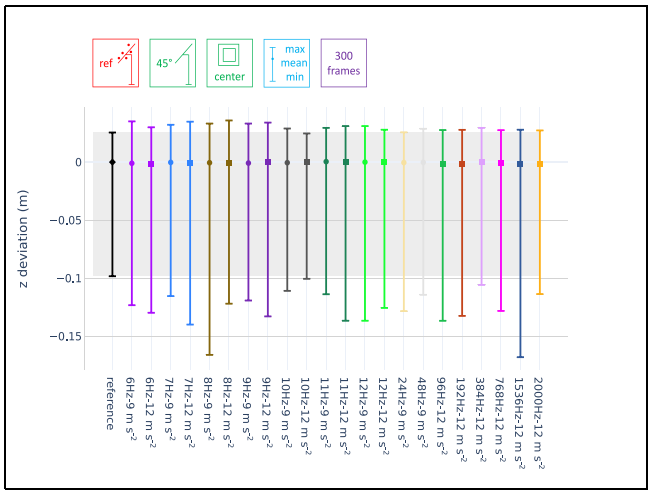


**FIGURE 12.** Deviation of $z$ for each point of the center area of the 45° target from the reference. The reference is the mean coordinates of each point, shown as green points in Fig. 7a.

as the reference. Nevertheless, experiments with the highest deflection, at up to 10 Hz, have many frames with a lower count in the lowest ring, number 31. Hence, some of the points on ring 31 dropped off the target.

Multiple rings could only drop off due to a change of the viewing angle caused by deformation of the lidar unit itself. This is because the distance between two rings is about 5.5 cm at the target's distance, whereas the peak-to-peak displacement of the OS1-64 in z-direction is only 1.2 cm at the maximum (Fig. 3). Furthermore, our experiments show that points on ring 30 did not drop off, while, however, points on ring 31 dropped off the target. Fig. S3 of the supplements shows that the number of points on ring 30 is independent of the vibration frequency.

Fig. 12 shows deviations in $z$-direction between the points measured on the target center and the mean reference point cloud. The figure shows that all loads lead to a higher displacement in $z$ direction compared to the normal noise of the static reference. The mean of $z$ deviations over the center target was used since $z$ deviations of single points are completely different for each point, as can be seen in Fig. S4 of the supplements.

Fig. 13 shows that all loads lead to higher standard deviations of distances from ground-truth over single point clouds. In addition, the range of those standard deviations is bigger for all loads. We can thus conclude that the standard deviation varies more during vibration than in comparison to the static reference.

## V. CONCLUSION

In this study, we investigated the effects of vertical vibration on the housing and on the point clouds recorded by an Ouster OS1-64 automotive lidar. The resonance detected at 1425 Hz seems to have no pronounced negative effect on the point cloud, indicating that the sensor housing was made sufficiently stiff.

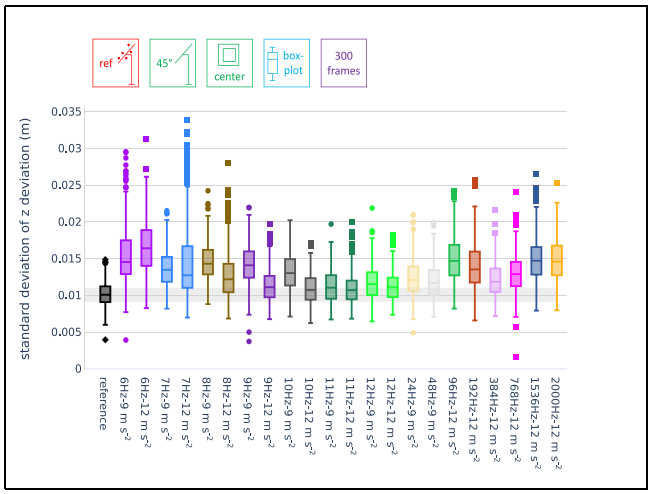


**FIGURE 13.** Boxplots of standard deviations of distances between measured point clouds and mean reference point cloud. All points of the defined target center are considered. The standard deviations of distances are calculated on a frame-by-frame basis.

An information loss takes place during vibration, which is, however, mostly independent of the frequency and is indeed surprisingly consistent from experiment to experiment. Hence, rough road surfaces and vibrating vehicle components may lead to a reduced number of points in the point clouds. More points were only lost at the experiment with the harshest conditions, at 6 Hz and 12 $\mathrm{m\,s^{-2}}$. The cause of this loss is unknown, and might be due to some internal processing which was not accessible during the experiments. This information loss can prove problematic if they randomly accrue as a cluster and hence might negatively impact object detection algorithms.

In some cases, as in Fig. 10, the opposite effect occurs, wherein an information gain takes place through vibration. There are more points hitting the target while the lidar sensor moves vertically. In this case, the effect of vibration is thus slightly positive. This is despite the fact that, in reality, this effect is likely negligible for object detection.

IMUs are well established in vehicles and it is therefore advisable to use them to detect vibrations. Even the internal IMU of the lidar unit proved to be reliable up to 50 Hz. It follows then, that only vibrations caused by uneven road surfaces — and not by vibrating vehicle components — may be detected in this fashion.

The retroreflective targets proved to be problematic and should be avoided in future experiments. This effect is less pronounced in road signs (see the Fig. S2 in the supplements) due to their spherical reflectors as opposed to the prism-shaped ones in the reflective foil. The updated data sheet from Ouster now provides an accuracy range of ±10 cm for retroreflectors [22]. We investigated the count of points on the target's lowest ring, which is close to the edge, as an example of a material and an IMU independent method for detecting vibration.

Overall, the lidar unit is well equipped to deal with frequencies from 6 to 2000 Hz, and up to 12 $\mathrm{m\,s^{-2}}$. Acceleration data from IMUs can help to determine a confidence metric in the perception system, as a loss of information took place during vibration. The cause of the information loss still needs to be determined, but due to the random spatial distribution of the loss, it might not be of concern.

## VI. DATA AND SOFTWARE AVAILABILITY

We provide the data that we collected and analyzed on Zenodo: https://doi.org/10.5281/zenodo.5770259. The Python package required for analytics is available on github: https://github.com/virtual-vehicle/pointcloudset.

## APPENDIX

As the numerical integration may lead to unwanted errors, a few steps must be taken to ensure the results are as expected.

1) remove the low frequency components by subtracting a low degree polynomial
2) linearization errors removed by up-sampling the raw data by at least four times the original sampling frequency 8 kHz
3) integration is done using the trapezium method and followed by down sampling to the original sampling frequency
4) a high pass filter at 1 Hz is used to remove the integration constant.

The integration was done in the time signal calculator of the Simcenter Test.Lab Software version 2020 so that calculations could be made directly in the measuring software.

## ACKNOWLEDGMENT

The authors would like to express their thanks to David Ritter for conducting the time-of-flight camera measurements of the retroreflective foil and the road sign. The publication was written at Virtual Vehicle Research GmbH in Graz, Austria.

## REFERENCES

[1] L. Liu *et al.*, "Computing systems for autonomous driving: State of the art and challenges," *IEEE Internet Things J.*, vol. 8, no. 8, pp. 6469–6486, Apr. 2021. [Online]. Available: https://doi.org/10.1109/JIOT.2020.3043716

[2] T. Goelles, B. Schlager, and S. Muckenhuber, "Fault detection, isolation, identification and recovery (FDIIR) methods for automotive perception sensors including a detailed literature survey for LiDAR," *Sensors*, vol. 20, vol. 13, 2020, Art. no. 3662. [Online]. Available: https://doi.org/10.3390/s20133662

[3] Y. Hua, S. Wang, B. Li, G. Bai, and P. Zhang, "Dynamic modeling and anti-disturbing control of an electromagnetic mems torsional micromirror considering external vibrations in vehicular LiDAR," *Micromachines*, vol. 12, no. 1, 2021, Art. no. 69. [Online]. Available: https://doi.org/10.3390/mi12010069

[4] J. Grahmann, R. Schroedter, O. Kiethe, and U. Todt, "Vibration analysis of micro mirrors for LiDAR using on-chip piezo-resistive sensor," in *Proc. MOEMS Miniaturized Syst. XIX*, vol. 11293, 2020, pp. 34–45. [Online]. Available: https://doi.org/10.1117/12.2551600

[5] C. Periu, A. Mohsenimanesh, C. Laguë, and N. McLaughlin, "Isolation of vibrations transmitted to a LiDAR sensor mounted on an agricultural vehicle to improve obstacle detection," *Can. Biosyst. Eng.*, vol. 55, no. 1, pp. 2.33–2.42, 2013. [Online]. Available: https://doi.org/10.7451/CBE.2013.55.2.33

[6] R. Wang, B. Wang, M. Xiang, C. Li, S. Wang, and C. Song, "Simultaneous time-varying vibration and nonlinearity compensation for one-period triangular-FMCW LiDAR signal," *Remote Sens.*, vol. 13, no. 9, 2021, Art. no. 1731. [Online]. Available: https://doi.org/10.3390/rs13091731

[7] J. Cao, X. Cheng, J. Shang, and Y. He, "Analysis of the effect of vibration on vehicle LiDAR system," *Opt. Eng.*, vol. 59, no. 11, 2020, Art. no. 114101. [Online]. Available: https://doi.org/10.1117/1.OE.59.11.114101

[8] M. Harter and J. Hildebrandt, "Vibrations in automotive radar systems," in *Proc. IEEE MTT-S Int. Conf. Microw. Intell. Mobility (ICMIM)*, San Diego, CA, USA, 2016, pp. 1–4. [Online]. Available: https://doi.org/10.1109/ICMIM.2016.7533829

[9] F. Hau, F. Baumgärtner, and M. Vossiek, "Influence of vibrations on the signals of automotive integrated radar sensors," in *Proc. IEEE MTT-S Int. Conf. Microw. Intell. Mobility (ICMIM)*, 2017, pp. 159–162. [Online]. Available: https://doi.org/10.1109/ICMIM.2017.7918881

[10] F. Hau, F. Baumgärtner, and M. Vossiek, "The degradation of automotive radar sensor signals caused by vehicle vibrations and other nonlinear movements," *Sensors*, vol. 20, no. 21, 2020, Art. no. 6195. [Online]. Available: https://doi.org/10.3390/s20216195

[11] H. Ma and J. Wu, "Analysis of positioning errors caused by platform vibration of airborne LiDAR system," in *Proc. 8th IEEE Int. Symp. Instrum. Control Technol. (ISICT)*, 2012, pp. 257–261. [Online]. Available: https://doi.org/10.1109/ISICT.2012.6291650

[12] X. Song, C. Chen, B. Liu, J. Xia, and S. Stanic, "Design and implementation of vibration isolation system for mobile doppler wind LiDAR," *J. Opt. Soc. Korea*, vol. 17, no. 1, pp. 103–108, Feb. 2013. [Online]. Available: https://doi.org/10.3807/JOSK.2013.17.1.103

[13] A. Pacala. "Putting the OS1 Through a Battery of Reliability Tests." 2019. [Online]. Available: https://ouster.com/blog/putting-the-os1-through-a-battery-of-reliability-tests/

[14] "Ouster OS1-64 (gen1)," Data Sheet, Ouster, Inc., San Francisco, CA, USA, 2019. [Online]. Available: https://data.ouster.io/downloads/datasheets/datasheet-revd-v2p0-os1.pdf

[15] D. Thorby, "13—Vibration testing," in *Structural Dynamics and Vibration in Practice*, D. Thorby, Ed. Oxford, U.K.: Butterworth-Heinemann, 2008, pp. 367–385. [Online]. Available: https://doi.org/10.1016/B978-0-7506-8002-8.00013-4

[16] (Stanford Artif. Intell. Lab., Stanford, CA, USA). *Robotic Operating System*. (May 2018). [Online]. Available: https://www.ros.org

[17] T. Goelles, B. Schlager, S. Muckenhuber, S. Haas, and T. Hammer, "Pointcloudset: Efficient analysis of large datasets of point clouds recorded over time," *J. Open Source Softw.*, vol. 6, no. 65, 2021, Art. no. 3471. [Online]. Available: https://doi.org/10.21105/joss.03471

[18] "RIEGL VZ-6000 3D ultra long range terrestrial laser scanner with online waveform processing." Data Sheet, RIEGL Laser Meas. Syst. GmbH, Horn, Austria, 2020. [Online]. Available: http://www.riegl.com/uploads/tx_pxpriegldownloads/RIEGL_VZ-6000_Datasheet_2020-09-14.pdf

[19] "Operating & processing software RiSCAN pro for RIEGL 3D laser scanners' RiSCAN pro," Data Sheet, RIEGL Laser Meas. Syst. GmbH, Horn, Austria, 2020. [Online]. Available: http://www.riegl.com/uploads/tx_pxpriegldownloads/RiSCAN-PRO_DataSheet_2020-10-07_01.pdf

[20] Y. Shi, L. Fang, R. Li, D. Guo, S. Zhang, and Q. Tang, "Processing method of acceleration signal with zero drift," in *Proc. J. Phys. Conf. Series*, vol. 1952, no. 3, Jun. 2021, Art. no. 032061. [Online]. Available: https://doi.org/10.1088/1742-6596/1952/3/032061

[21] (Ouster, Inc., San Francisco, CA, USA). *Software User Guide—Release V1.13.0*. (2019). [Online]. Available: https://data.ouster.io/downloads/software-user-manual/software-user-manual-v1p13.pdf

[22] "Ouster OS1-64 Datasheet: Mid-range high-resolution imaging lidar," Data Sheet, Ouster, Inc., San Francisco, CA, USA, 2021. [Online]. Available: https://data.ouster.io/downloads/datasheets/datasheet-revd-v2p1-os1.pdf